JGR Atmospheres

Key Points:

- Aerosol physical and chemical characteristics from a three-wavelength Raman lidar and airborne microphysical and chemical sensors
- A retrieval approach based on Tikhonov regularization is applied to lidar measurements to infer aerosol size and microphysical properties
- Ensemble back-trajectory modeling and measurements combined to determine aerosol types and origins and their source–receptor relationships

Correspondence to:
P. Di Girolamo,
paolo.digirolamo@unibas.it

Measurements of Aerosol Size and Microphysical Properties: A Comparison Between Raman Lidar and Airborne Sensors

P. Di Girolamo[1] , **B. De Rosa[1,2]**, **D. Summa[1,2]** , **N. Franco[1]**, and **I. Veselovskii[3]**

[1]Scuola di Ingegneria, Università degli Studi della Basilicata, Potenza, Italy, [2]Istituto di Metodologie per l' Analisi Ambientale, Consiglio Nazionale delle Ricerche, Tito Scalo, Italy, [3]Prokhorov General Physics Institute of the Russian Academy of Sciences, Moscow, Russia

Abstract This manuscript compares measurements of aerosol size distributions and microphysical properties retrieved from the Raman lidar BASIL with those obtained from a series of aircraft sensors during HyMeX-SOP1. The attention is focused on a measurement session on 02 October 2012, with BASIL measurements revealing the presence of a lower aerosol layer extending up to 3.3 km and an elevated layer extending from 3.6 to 4.6 km. Aerosol size distribution and microphysical properties are determined from multi-wavelength particle backscattering and extinction profile measurements through a retrieval approach based on Tikhonov regularization. A good agreement is found between BASIL and the microphysical sensors' measurements for all considered aerosol size and microphysical properties. Specifically, BASIL and in-situ volume concentration values are in the range 2–5 $\mu m^3\ cm^{-3}$ in the lower layer and in the range 1–3.5 $\mu m^3\ cm^{-3}$ in the upper layer. Values of the effective radius values from BASIL and the in-situ sensors are in the range 0.2–0.6 µm in both the lower and upper layer. Aerosol size distributions are determined at 2.2, 2.8, 4 and 4.3 km, with a good agreement between the Raman lidar and the microphysical sensors at all considered heights. We combined these size and microphysical results with Lagrangian back-trajectory analyses and chemical composition measurements. From this combination of datasets we conclude that aerosol particles below 3 km were probably originated by wildfires in North America and/or by anthropogenic activities in North-Eastern Europe, while aerosols above 3 km were also probably originated by wildfires in North America.

Plain Language Summary Physical and chemical properties of aerosol particles obtained from a multi-wavelength Raman lidar and airborne in-situ microphysical and chemical sensors. A retrieval scheme exploiting Tikhonov's inversion is applied to the lidar measurements to infer aerosol size and microphysical properties. A good agreement between the lidar and the in-situ sensors is found for all considered parameters. Ensemble back-trajectory modeling and measurements are combined to determine the types and origin of the aerosol particles and source-receptor relationships.

1. Introduction

Aerosols are suspended particles including a large variety of species, such as minerals, sea salt, dust, nitrates, sulfates, water and carbon, which may greatly vary in size (Bonsang et al., 1992; Leck & Bigg, 2005a, 2005b). Aerosols are directly injected in the atmosphere as particles (primary aerosols) or may form in it through chemical reactions involving gaseous species (secondary aerosols). While primary aerosols are generated in all sizes, secondary aerosols are primarily generated in the sub-micron-meter size range (<0.1 µm).

Tropospheric aerosols represent an important component of the Earth's radiation budget. Atmospheric scattering and absorption of both solar and planetary radiation are strongly dependent on aerosol concentration (Albrecht, 1989; Charlson et al., 1992; IPCC, 2007; Twomey, 1977). Additionally, aerosol concentrations may influence nucleation and cloud microphysical processes (among others. Khain et al., 1999; Thompson & Eidhammer, 2014).

Aerosol mass and particle concentrations are characterized by a high space and time variability. Consequently, aerosol radiative forcing is ultimately affected by larger uncertainties than greenhouse gases' radiative forcing. This is due to the shorter lifetime of atmospheric aerosols as compared to the major greenhouse gases. In order to quantitatively estimate aerosol radiative forcing, spatially and temporally resolved information on atmospheric aerosol chemical, size, microphysical and radiative properties are necessary (Boucher et al., 2013; Rap, 2013).

Validation: P. Di Girolamo, B. De Rosa, D. Summa, N. Franco, I. Veselovskii
Visualization: P. Di Girolamo, B. De Rosa, D. Summa, I. Veselovskii
Writing – original draft: P. Di Girolamo, B. De Rosa
Writing – review & editing: P. Di Girolamo

Among these are the real and imaginary part of the refractive index, the volume concentration, the effective radius, the single scattering albedo and the aerosol size distribution.

Vertical profiles of aerosol size and microphysical properties can be measured by few techniques, with airborne in-situ sensors probably representing the most effective source of data. However, the exploitation of in-situ sensors is costly and complex, and this ultimately translates into a limited use of such sensors. Remote sensing techniques, as multi-wavelength Raman lidars, have a strong potential, but their performance needs to be validated against independent measurements.

Lidar measurements of the aerosol optical properties have been reported since the nineteen-sixties, with pioneering measurements by Fiocco and Grams (1964) and Elterman (1966). During the seventies and eighties, single-wavelength particle backscatter profile measurements were primarily reported. In those research efforts, particle backscattering coefficient profiles were determined from single-wavelength elastic signals through the application of different approaches (Di Girolamo et al., 1995, 1999; Fernald, 1984; Klett, 1981, 1985). Later, in the nineties, particle extinction coefficient profile measurements became available thanks to the acquired capability to measure Raman backscatter lidar signals from N_2 and O_2 molecules (Ansmann et al., 1990, 1992).

The possibility to determine aerosol size and microphysical properties from multi-wavelength Raman lidar measurements of the aerosol backscattering and extinction coefficient and depolarization ratio profiles has been demonstrated by a variety of authors (Freudhenthaler et al., 2009; Müller et al., 1999, 2007; Veselovskii et al., 2002, 2010, 2018). Retrieved profiles of aerosol size and microphysical properties can be combined with co-located atmospheric humidity and temperature profiles to characterize aerosol–cloud interaction mechanisms (Di Girolamo et al., 2008, 2018; Di Girolamo, Summa, Cacciani et al., 2012; Wulfmeyer et al., 2005).

The Raman lidar system BASIL developed at Scuola di Ingegneria, University of Basilicata, provides accurate three-wavelength measurements of aerosol optical coefficients with high vertical and temporal resolution. BASIL measurements can and have been used for the determination of aerosol size distribution and microphysical properties (Di Girolamo, Summa, Bhawar, et al., 2012; Veselovskii et al., 2010). In the present paper, size properties, namely the volume concentration, the effective radius, the parameters of a bi-trimodal size distribution, and microphysical properties, namely the real and imaginary part of the refractive index, are determined from three-wavelength particle backscattering and two-wavelength particle extinction profile measurements. A retrieval approach based on Tikhonov regularization has been applied to the multi-wavelength BASIL measurements. Results are compared with measurements from microphysical sensors on-board the French research aircraft Avions de Transport Régional (ATR)-42. Reported measurements, collected during the First Special Observation Period (SOP1) of the Hydrological Cycle in the Mediterranean Experiment (HyMeX), represent a unique data set to assess the performance and accuracy of the inversion approaches applied to infer particle size and microphysical properties from multi-wavelength lidar measurements.

HyMeX-SOP1 took place in the North-Western Mediterranean basin in time period September–November 2012. The experiment involved a large ensemble of instruments located in a variety of measurement sites. In the frame of HyMeX-SOP1, BASIL was placed at a coastal observational site facing the Gulf of Lion in Southern France (Candillargues, Lat: 43.61°N, Long: 4.07°E, Elev: 1 m). During HyMeX-SOP1, the ATR-42 was equipped with several sensors for the characterization of turbulence and aerosol/cloud microphysical processes. The research aircraft performed approximately 60 flight hours, 8 of which being funded by the European Commission through a specific project of seventh Framework Program (EUropean Facility for Airborne Research (EUFAR), WaLiTemp). The aircraft flight pattern included vertical spirals (hippodromes). Because of the imposed restrictions to air-traffic, hippodromes were centered approximately 20 km East of the Raman lidar site.

Measurements benefited from a large aerosol outburst primarily generated by the large and intensive wildfires taking place in North America throughout the month of September 2012 associated with the exceptional summer-autumn drought over the central Great Plains.

The paper outline is as follows. Section 2 describes the different considered instruments. Section 3 illustrates the methodology used to infer aerosol size distributions and microphysical properties from three-wavelength particle backscattering and extinction coefficient profile measurements. Section 4 compares retrievals from the multi-wavelength Raman lidar measurements with in-situ sensors' measurements. Section 5 summarizes the results and gives some perspectives for future activities.

2. Instruments

2.1. BASIL

The Raman lidar BASIL includes a Nd: Yttrium-Aluminium-Garnet laser source equipped with frequency doubling and tripling crystals and emitting pulses at 1,064, 532 and 355 nm, with a frequency repetition rate of 20 Hz. The receiver is developed around a Newtonian telescope, with a primary mirror diameter of 0.45 m. Two 0.05 m diameter lenses are also included in the receiver for the collection of the elastic echoes at 532 and 1064 nm. BASIL can provide accurate measurements of atmospheric water vapor and temperature profiles, with high temporal and vertical resolution, both during the day and at night, based on the exploitation of the vibrational and rotational Raman lidar techniques, respectively, in the ultraviolet (Di Girolamo et al., 2004, 2006, 2009; De Rosa, Di Girolamo, & Summa, 2018; De Rosa, Di Girolamo, Summa, Flamant et al., 2018; De Rosa et al., 2020). Besides water vapor and temperature profiles, BASIL also carries out vertical profile measurements of a variety of particle optical parameters. These are the backscattering coefficient at 355, 532, and 1064 (referred to in the following as 3β), the particle extinction coefficient at 355 and 532 (referred to in the following as 2α), and the particle depolarization ratio at 355 and 532 nm. These measurements are used in the paper to infer aerosol size and microphysical properties. Before and after HyMeX-SOP1, BASIL participated to a variety of other international field deployments (among others, Di Girolamo, Summa, Bhawar, et al., 2012; Di Girolamo et al., 2018; Di Girolamo et al., 2020; Summa et al., 2018; De Rosa, Di Girolamo, & Summa, 2018; De Rosa, Di Girolamo, Summa, Flamant et al., 2018).

2.2. Instruments on Board ATR-42 Aircraft

Several microphysical and chemical sensors with in-situ measurement capability are included in the instrumental ensemble hosted by the ATR-42 atmospheric research aircraft, operated by Service des Avions Français Instrumentés pour la Recherche en Environnement. During HyMeX-SOP1, the research aircraft was based at Montpellier airport. 28 flights were carried out between 11 September and 4 November 2012.

An optical particle counter (hereafter called OPC), produced by GRIMM Aerosol Technik GmbH, provides measurements of the aerosol size distribution in the radii range 350–2,500 nm (Heim et al., 2008). The measurement principle relies on a 683 nm laser beam from a diode laser sent over the aerosol sample, with the scattered radiation being detected by a photo-sensor module including 31 size bins. Total number concentration is obtained by integrating the number concentration size distribution over the above specified size range. The OPC is specifically designed for airborne exploitation (Sullivan et al., 2014).

A Scanning Mobility Particle Sizer (hereafter called SMPS) is used to measure the size distributions of aerosol particles in the radii range 20–485 nm. The SMPS operation principle relies on measurements of accumulated charge over a specific target, with the aerosols being first charged and then subjected to an electrical field (Crumeyrolle et al., 2010). The combined use of the measurements from the SMPS and the OPC allows us determining aerosol size distributions throughout the radii range 20 nm–2.5 µm. The upper limit of the in-situ measurements prevents from a proper characterization of large and giant aerosols, which represent an important fraction of the sounded aerosol particles. This upper size detection limit is absent in the multi-wavelength Raman lidar retrievals, which can properly reproduce aerosol size distributions in the radii range 0.075–10 µm (Veselovski et al., 2012).

A compact time-of-flight Aerosol Mass Spectrometer (C-ToF-AMS, Aerodyne, Drewnick et al., 2005; Canagaratna et al., 2007) provides mass concentration measurements of the non-refractory submicron fraction of the aerosol population. The AMS was used to quantify species such as ammonium sulfate and bisulphate, ammonium chloride, ammonium nitrate, and organic compounds. The SMPS represents the primary source of information on aerosol composition considered in the present research effort. Information on black carbon is unfortunately missing. Because of the imposed restrictions to air-traffic, sensors' operation was not possible over the vertical of the lidar site. A specific flight pattern was conceived for the purposes of the EUFAR project "WaLiTemp," with the aircraft spiraling up and down around a central point located approximately 20 km East of the Raman lidar site. "WALiTemp" flights took place on 13 September, 02 and 29 October and 05 November 2012, with spiral diameters of 5–10 km and ascent and descent speeds of approximately 2.5 m/s.

3. Methodology

An appropriate characterization of the space and time variability of aerosol size and microphysical properties is of paramount importance for understanding aerosol effects on climate. The most frequently used parameters in this regard are: the volume concentration, the mean and effective radius and the real and imaginary part of the refractive index. This set of microphysical properties can, for example, be used to estimate the single-scattering albedo, which is a key parameter for the assessment of aerosol radiative forcing in climate studies (Canagaratna et al., 2007).

Specific retrieval algorithms can be used to determine these parameters from multi-wavelength Raman lidar measurements. The measured optical parameters and the retrieved size and microphysical properties are related through non-linear and not analytically solvable, integral equations (Fredholm equations of the first kind). This represents the main difficulty associated with the application of these algorithms. Numerical solutions of these equations are strongly dependent on the statistical and systematic uncertainties affecting the ingested input data. Additionally, solutions are not unique. A careful check of the retrieved results is therefore necessary because solutions may be mathematically correct, but still not reflect and properly represent the real physical conditions.

In the present research effort, aerosol size and microphysical properties are obtained from three-wavelength measurements of the particle backscattering coefficient and two-wavelength measurements of the particle extinction coefficient through a retrieval scheme based on Tikhonov regularization. The retrieval approach assumes particles to be spherical, with kernel functions being constructed accordingly. Veselovskii et al. (2002) demonstrated that an input data set including particle backscattering coefficient profiles at 355, 532, and 1064 nm ($\beta_{355}(z)$, $\beta_{532}(z)$ and $\beta_{1064}(z)$, respectively), and particle extinction coefficient profiles at 355 and 532 nm ($\alpha_{355}(z)$ and $\alpha_{532}(z)$, respectively), that is, $3\beta + 2\alpha$, may be used to determine a variety of aerosol size and microphysical properties. Among others, the number, surface and volume concentration, the mean and effective radius, the size distribution and the real and imaginary part of the refractive index. Veselovskii et al. (2002) also demonstrated that reliable retrievals are possible only if the overall uncertainty (statistical and/or systematic) affecting particle backscatter profile measurements is smaller than 5% and the uncertainty affecting particle extinction profile measurements is smaller than 10%. Veselovskii et al. (2002) also assessed that in the application of the $3\beta + 2\alpha$ approach, a 10% uncertainty affecting the input optical data translates into a 20% uncertainty in the retrieved mean radius, a 10%–20% uncertainty in the retrieved effective radius, a 5%–10% uncertainty in the retrieved volume concentration and an uncertainty of 0.05% and 50% in the retrieved real and imaginary part of the refractive index, respectively.

4. Results

4.1. Particle Backscattering and Extinction Profiles From BASIL

We focused our attention on the Raman lidar and in-situ measurements carried out on 02 October 2012. Measurements by BASIL started on this day at 16:00 Universal Time Coordinated (UTC) and ended at 24:00 UTC. Figure 1 shows the flight pattern of the ATR-42 on this day. The plane took off at 19:43 UTC from Montpellier airport to reach few minutes later an area in the proximity of the observational site in Candillargues. Unfortunately, because of the imposed restrictions to air-traffic, the central location of the aircraft flight pattern, including spirals up and down, was displaced approximately 20 km East of the lidar site (spiral center coordinates: Lat: 43°65 N and Long: 4°30 E). At 20:57 UTC the aircraft ended its spiral up, reaching a height of 6 km, and began to make the descending spiral. At 22:22 UTC the plane landed in Montpellier airport.

The color map in Figure 2 shows the time evolution of the aerosol backscattering coefficient measurements at 355 nm, $\beta_{355}(z)$, from BASIL covering ∼ 4 hr time interval from 19:20 to 23:40 UTC. The figure clearly reveals a lower aerosol layer extending up to ∼3 km and an upper layer above, extending up to ∼4.5 km.

For the purpose of applying the retrieval scheme and determining aerosol size distribution and microphysical properties, we focused our attention on a time interval covering the central part of the measurement session, characterized by large aerosol concentrations. Additionally, in order to get low enough statistical uncertainties for the retrieval approach to be properly applied, a 2 hr averaging time interval from 20:00 to 22:00 UTC was considered for both the particle backscattering ($\beta_{355}(z)$, $\beta_{532}(z)$ and $\beta_{1064}(z)$) and the extinction coefficient ($\alpha_{355}(z)$
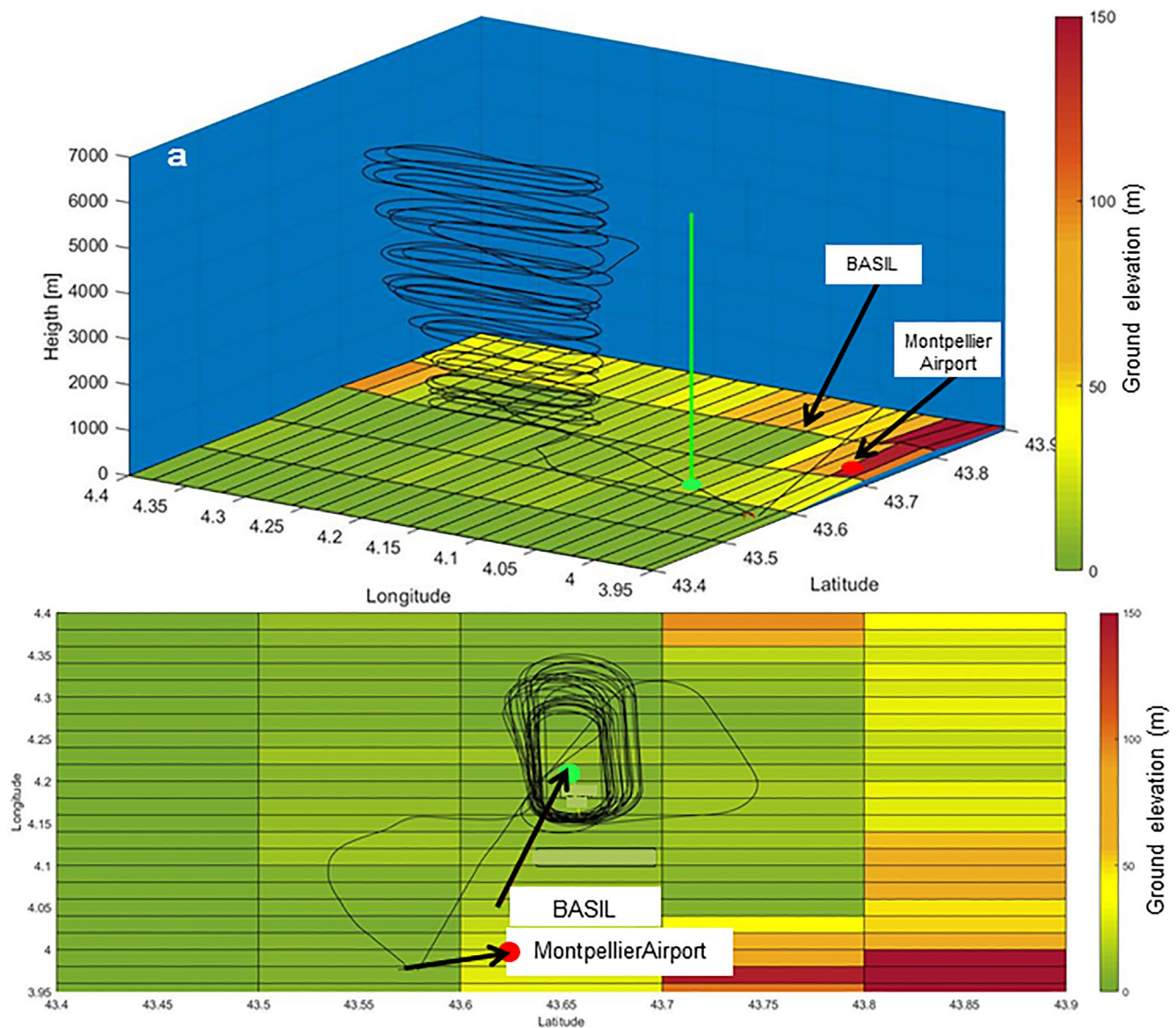
Figure 1. ATR-42 flight pattern from 19:43 to 22:22 UTC (panel a: 3-D image, panel b: horizontal section). The lidar system BASIL is represented as a green dot and line in panel (a) and as a green dot in panel (b), while Montpellier airport is represented as a red dot in both panels. The color scale in both figure panels represents the ground elevation.

and $\alpha_{532}(z)$) profiles. These profiles, illustrated in Figure 3, more clearly reveal the presence of a lower aerosol layer, extending up to 3.3 km, and an elevated aerosol layer extending from 3.6 to 4.6 km.

For the purpose of reducing the statistical uncertainty affecting the different optical parameters, backscattering coefficient profiles were vertically smoothed to achieve a vertical resolution of 150 m, while extinction coefficient profiles were vertically smoothed to achieved a vertical resolution of 300 m. The consideration of a 2 hr integration time and the vertical smoothing allows achieving uncertainties on backscattering and extinction coefficient profiles smaller than 10%. As we illustrated above, these low uncertainties are required to obtain accurate retrievals of the aerosol size and microphysical parameters. Backscattering coefficient profiles at 355 and 532 nm were determined through the application of the Raman lidar technique (Ansmann et al., 1992), obtained from ratioing the elastic signals at these wavelengths with the corresponding N_2 Raman signals at 386.6 and 607 nm, respectively. Backscattering coefficient profiles at 1064 nm were determined through the application of a Klett-modified method (Di Girolamo et al., 1995, 1999). In the application of this approach we assumed a
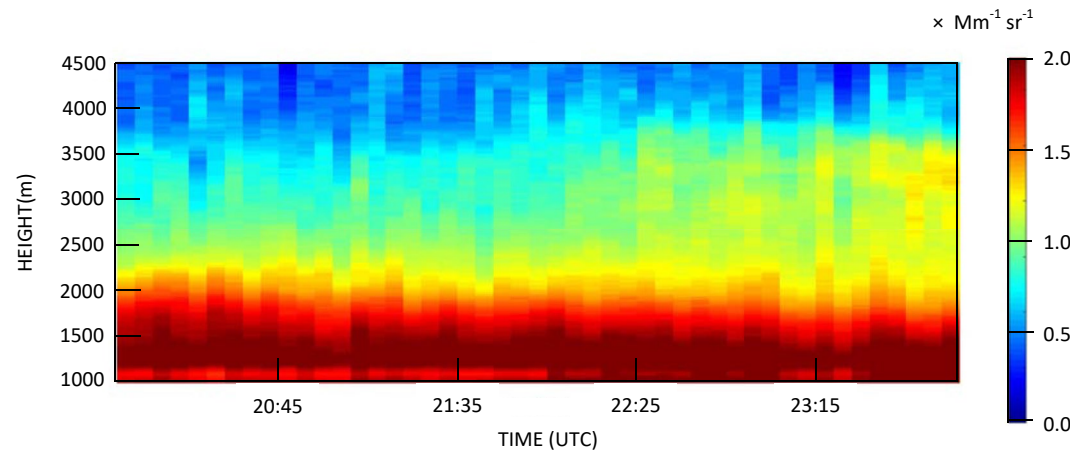
**Figure 2.** Time evolution of $\beta_{355}(z)$ over the time interval 19:20–23:40 UTC on 02 October 2012.

lidar ratio value of 50 sr and an aerosol-free region above 4,500 m. The extinction coefficient profiles at 355 and 532 nm were determined through the approach defined by Ansmann et al. (1990). In addition to the three wavelength particle backscattering and the two wavelength extinction coefficient profiles, Figure 3 also includes the profiles of the particle depolarization ratio at 355 nm, $\delta_{355}(z)$, and of the lidar ratio at 355 and 532 nm, $LR_{355}(z)$ and $LR_{532}(z)$, respectively. Even if both particle depolarization and lidar ratio profile measurements are not used in the retrieval scheme, their consideration is of paramount importance for the purpose of aerosol classification (Burton et al., 2012; Illingworth et al., 2015). Their vertical variability is carefully considered in the last section of the paper for the verification of the results.

4.2. Back-Trajectory Analysis in Combination With Aerosol Mass Spectrometer Measurements for the Assessment of Aerosol Origin and Composition

The NOAA Lagrangian ensemble back-trajectory model HYSPLIT (Draxler & Hess, 1998; Rolph et al., 2017; Stein et al., 2015) is applied to determine the origin of the investigated air masses and establish source–receptor relationships. The Lagrangian trajectory approach involves the calculation of air parcels movement back in time from the receptor site, which yields the back-trajectories of the parcels. Specifically, the ensemble trajectory model starts multiple backward trajectories from the lidar site location at the time of the reported lidar observations. In the HYSPLIT ensemble run, each trajectory is calculated considering an offset of the meteorological data by one grid point in the horizontal and by 0.01 sigma units in the vertical (~250 m). This leads to 27 ensemble member trajectories for all-possible 3D (latitude, longitude, height) offsets. The 27 members are created from three planes of nine trajectories, each plane at ±0.1 sigma (about 250 m). The nine trajectories on each plane represent all combinations of ± horizontal combinations in *x* and *y*. The use of an ensemble approach instead of a single trajectory approach is motivated by the demonstrated capability of a sufficiently large ensemble of trajectories to more correctly represent the behavior of real air particles (Stohl et al., 2002). The meteorological data used for the present HYSPLIT runs are taken from the Global Data Assimilation System (GDAS) Reanalysis. Uncertainties affecting back-trajectory analyses from Lagrangian models may originate from the input meteorological data, the internal model errors, the physics parameterizations, and the stochastic processes. Meteorology data and their horizontal resolution have the largest impact on model uncertainty. For the considered input meteorological data (GDAS), the uncertainty affecting the original location of the air parcels reaching the receptor site is of the order of 20% of the traveled distance (Stohl, 1988).

Figure 4 shows the 280 hr ensemble back-trajectory analysis starting at 06:00 UTC on 21 September 2012 and ending in Candillargues at 2,000 and 4,000 m at 22:00 UTC on 02 October 2012, these being the central heights of the aerosol layers observed by BASIL at the time of the observations.

The ensemble back-trajectory analyses reveal that air masses ending at a height of 2,000 m in Candillargues (Figure 4a) originated approximately 9–12 days earlier in a continental area in North-Eastern Europe or in North America. Air masses then moved over the North Atlantic Ocean for 5–7 days to finally lift up to a height of
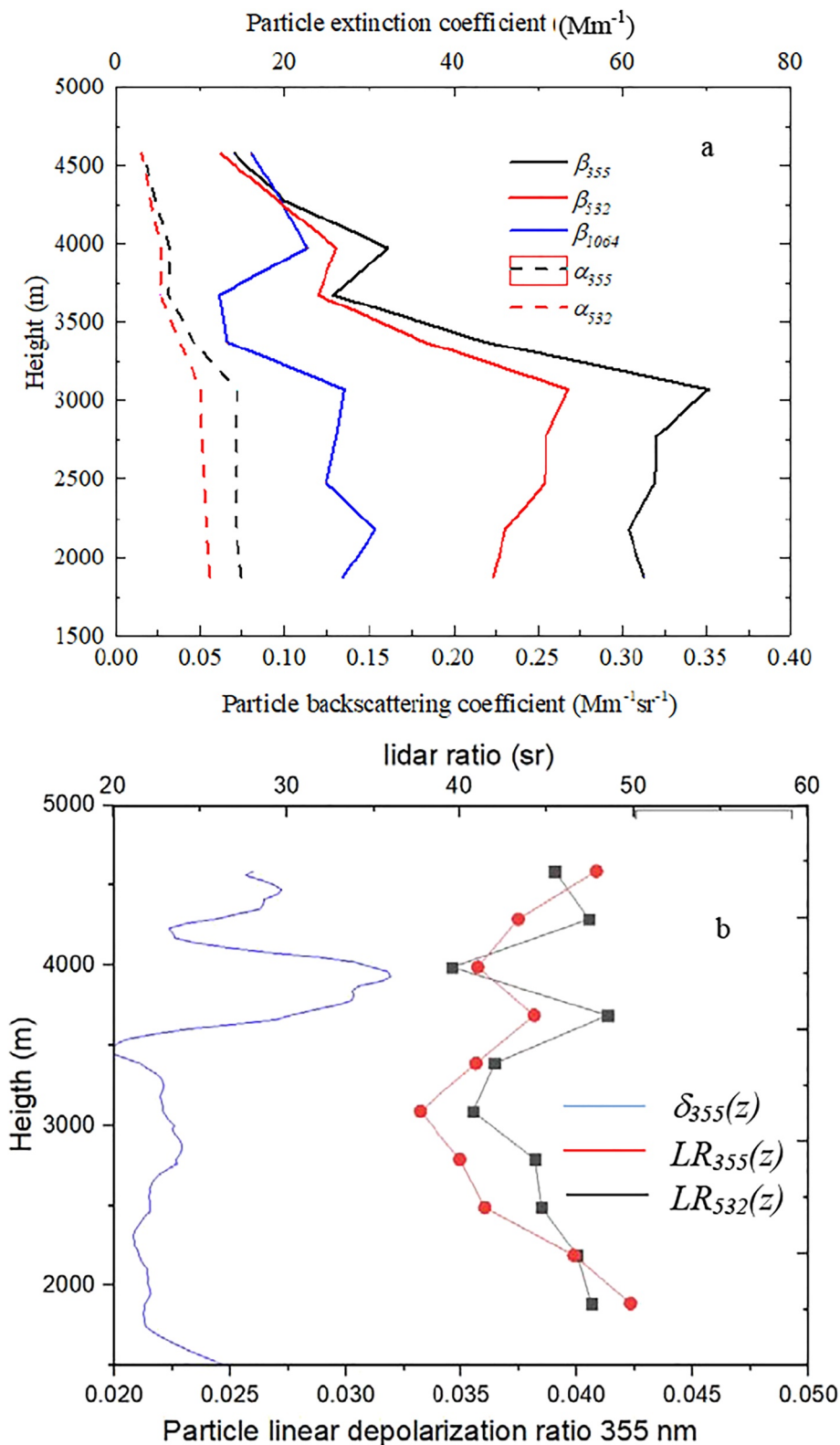
Figure 3. Vertical profiles of (a) the backscattering coefficients $\beta_{355}(z)$, $\beta_{532}(z)$ and $\beta_{1064}(z)$), and the extinction coefficients $\alpha_{355}(z)$ and $\alpha_{532}(z)$, (b) the particle linear depolarization ratio $\delta_{355}(z)$, and the lidar ratios $LR_{355}(z)$ and $LR_{532}(z)$.
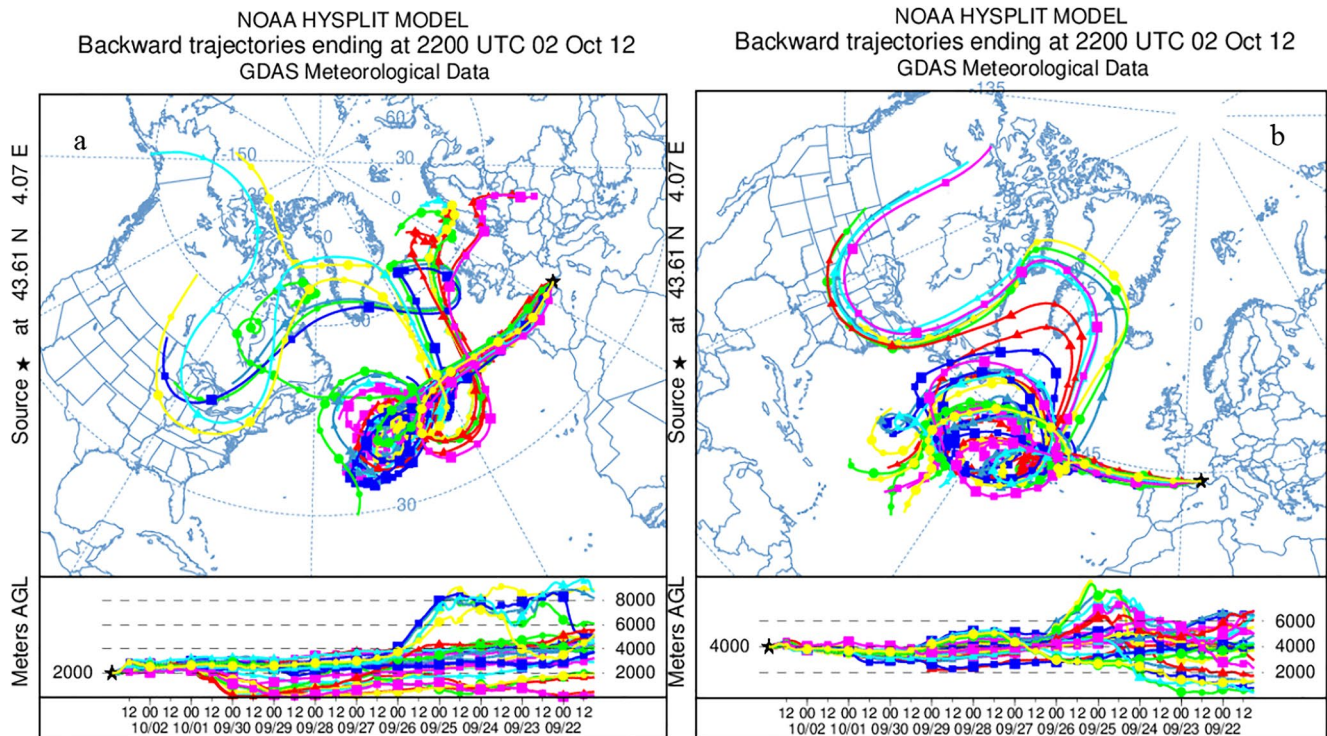
Figure 4. Ensamble back-trajectory analyses. Illustrated back-trajectories end in Candillargues at 2,000 (panel a) and 4,000 m (panel b) at 22:00 UTC on 02 October 2012 and started 280 hr earlier.

2,000 m in the proximity of the Azores Islands (around 28–30 September 2012), then crossing Northern Spain and finally reaching the lidar site on 02 October 2012. Ensemble back-trajectory analyses also indicate that the air masses ending at a height of 4,000 m in Candillargues (Figure 4b) originated approximately 11–12 days earlier over North-West America and traveled over the North Atlantic Ocean at a height between 2 and 3 km for most of the time to finally lift up and overpass Northern Spain 24–48 hr before reaching the lidar site.

The above ensemble back-trajectory analyses reveal the continental origin of the aerosols in both the lower and the upper layer. Air masses observed in both layers experienced a long traveling over a marine environment before reaching the observational site. One or both aerosol layers were most probably generated by the massive and extensive wildfires taking place in North America throughout the month of September 2012. In fact, dry conditions coupled with the abundance of dry fuels contributed to the widespread wildfire activity observed in autumn 2012, especially along the West Coast, the Northwest, and the northern Rockies.

More specifically, throughout the month of September 2012, an exceptional drought was concentrated over the central Great Plains, largely affecting Nebraska, Kansas, western Oklahoma, and south-eastern Colorado (Artusa, 2012). Areas of extreme drought combined with above-average temperatures and wind events produced large wildfire occurrences in Nebraska, South and North Dakota, Wyoming, Colorado, Oklahoma and north-western Minnesota during the month of September 2012, with Montana, South and North Dakota, and Minnesota experiencing the driest September on record since 1895. A monthly total of 1.08 million acres were burned by wildfires, this representing the third highest value for any September since 2000, while the year-to-date total of 8.80 million acres burned represents the second highest since 2000 (NOAA, 2012). These massive and extended wild fires and the oversea transport of their smokes strongly contributed to the high aerosol loading observed by BASIL in early October 2012.

During the flight on 02 October 2012 the AMS on board the ATR-42 reveals the presence of high concentrations of the main fine aerosols inorganic components, that is, NO_3, SO_4 and NH_4 (Figure 5), especially within the lower aerosol layer. These results are compatible with the aerosol sources identified with the back-trajectory analyses. In this regard it is to be specified that atmospheric NO_3, SO_4 and NH_4 are typically produced through chemical reactions involving particular precursor species such as NOx, SO_2, NH_3 and volatile organic compounds, which
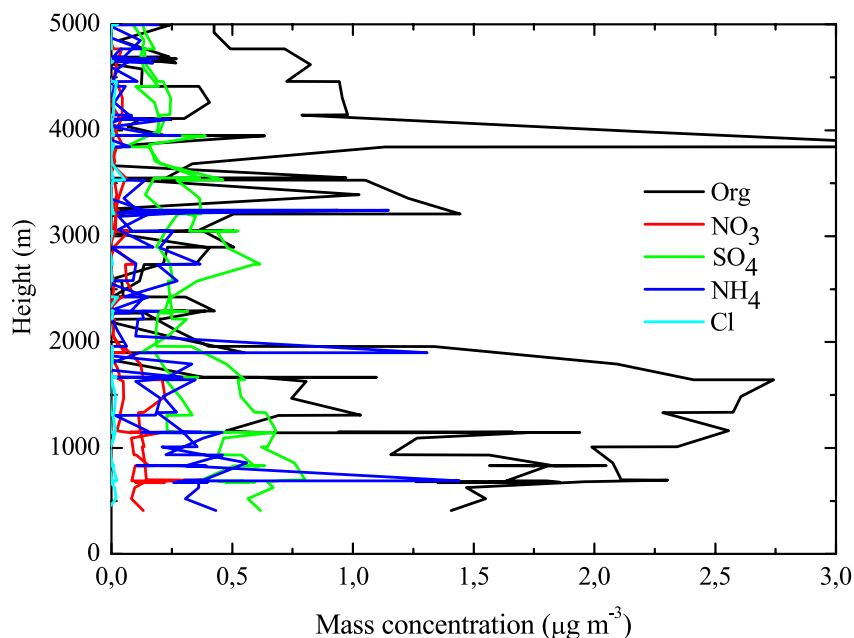
Figure 5. Aerosol Mass Spectrometer measurements. The different chemical species are identified by different colors. Measurements were carried out during both the aircraft ascending and descending phases.

can react with O_3 and OH to form secondary aerosols (Guerra et al., 2014; Kim et al., 2018; Marais et al., 2016). These precursor species are typically associated with combustion processes. Thus, high concentration of ammonium, sulfate and nitrate are often found in aerosols from combustion processes of natural or anthropogenic origin.

These aerosols are possibly associated with dust emissions from coal, oil and oil-shale burning from power plants and industrial areas in North-Eastern Europe, primarily the Baltic States (Carter, 1994; Yang et al., 2018), or smoke emissions from wildfires and dry fuel combustion in North America.

Figure 5 also reveals that organic aerosols (Org) represent a large fraction (up to 70%) of the particulate mass in the lowest 2 km. This fraction is possibly formed by primary organic aerosols directly produced by timber or fossil fuel combustion. The measured organic and inorganic aerosol components are compatible with emissions from biomass burning, as those taking place in North America in the weeks preceding the present observations.

Therefore, in the interpretation of the chemical properties and back-trajectory analyses of the aerosol particles observed in the lower layer we consider two possible hypotheses. A first hypothesis assumes the presence of aerosol particles generated by wildfires in North America, while a second hypothesis assumes anthropogenic emissions of pollution particles in North-Eastern Europe associated with the combustion of fossil fuels (coal, oil and oil-shale) from power plans and industrial activities. Both options are compatible with the reported chemical and back-trajectory data. These hypothesized compositions are also compatible with aerosol size distribution and microphysical properties measured by the in-situ sensors and retrieved from the three-wavelength Raman lidar measurements, which are illustrated in the continuation of the paper.

The AMS also shows increased values of the main fine aerosol inorganic components, that is, NO_3, SO_4 and NH_4, and organic components in the height interval 3,500–4,500 m, possibly resulting from precursor species generated by combustion processes (Figure 5). Air masses most probably originated over North America approximately 10–12 days earlier than being observed. In the path to the measurements site, air masses overpassed Northern Spain, without previously overpassing any specific polluted land area, which prevented from the formation of mixing processes, as possibly observed at other heights.
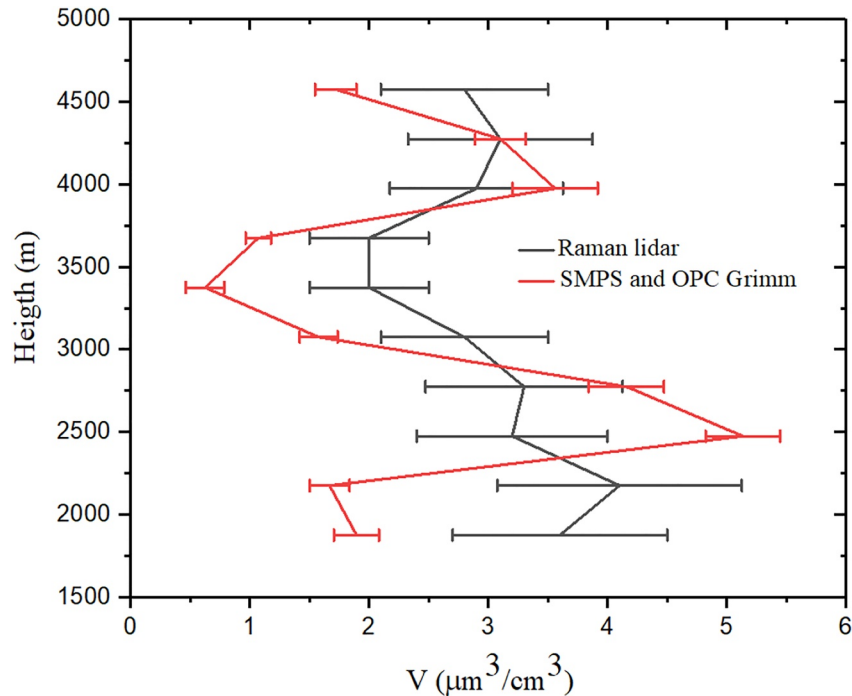
Figure 6. Comparison between BASIL and the aircraft in-situ sensors (SMPS + GRIMM OPC), expressed in terms of volume concentration measurements.

4.3. Application of the Retrieval Algorithm

Aerosol size and microphysical properties have been determined from the multi-wavelength Raman lidar data illustrated in Figure 3 based on the application of the inversion algorithm described in Section 3. Results from these retrievals are illustrated in the following and are compared with simultaneous measurements from the in-situ sensors on-board the ATR-42.

More specifically, Figure 6 illustrates the comparison of BASIL versus in-situ sensors expressed in terms of volume concentration profile measurements. The two instruments show comparable volume concentration values in both the lower layer (2–5 for the in-situ sensors and 3–4 $\mu m^3 \, cm^{-3}$ for the Raman lidar) and upper layer (1–3.5 for the in-situ sensors and 2–3 $\mu m^3 \, cm^{-3}$ for the Raman lidar).

The low level peak at 2,500 m in the in-situ volume concentration measurements is again presumably to be associated with either anthropogenic aerosols transported from industrial areas in North-Eastern Europe (Baltic States), generated in fossil fuel combustion processes from power plans and industrial areas, or with biomass-burning aerosols from wildfires in North America.

The high volume concentration peak value at 4,000 m is also likely associated with wildfires in North America, as already anticipated above. Retrievals from multi-wavelength Raman lidar measurements allow to properly reproduce the overall structures observed in the volume concentration profile from the in-situ sensors, with a small vertical mismatch (~300 m) in the height location of two peaks. In fact, the lower layer peak is at 2,500 m in the in-situ sensors' profile and at 2,200 m in the Raman lidar profile, while the upper layer peak is at 4,000 m for the in-situ sensors and at 4,300 m for the Raman lidar. The slight different values observed in terms of both volume concentration and vertical location of the peaks are possibly related to the circumstance that in-situ measurements are point measurements, with a limited degree of vertical integration, while Raman lidar data are vertically and temporally integrated over intervals coincident with their vertical and temporal resolution, respectively. On top of this, the ATR was spiraling up and down around a central position located approximately 20 km away from the lidar site.

Figure 7 illustrates the comparison expressed in terms of effective radius profiles between BASIL and the on-board in-situ sensors. Values from the in-situ sensors are in the range 0.35–0.6 μm, while values from BASIL
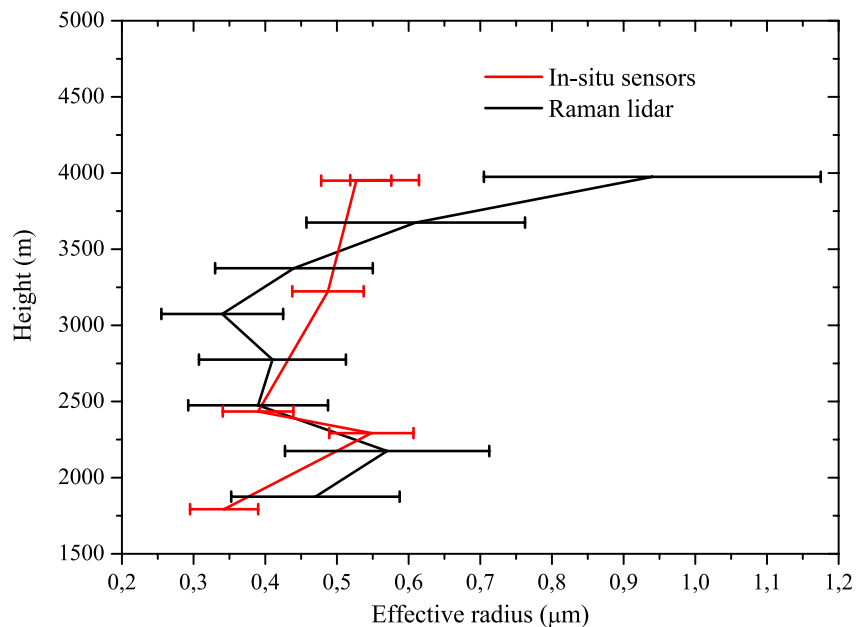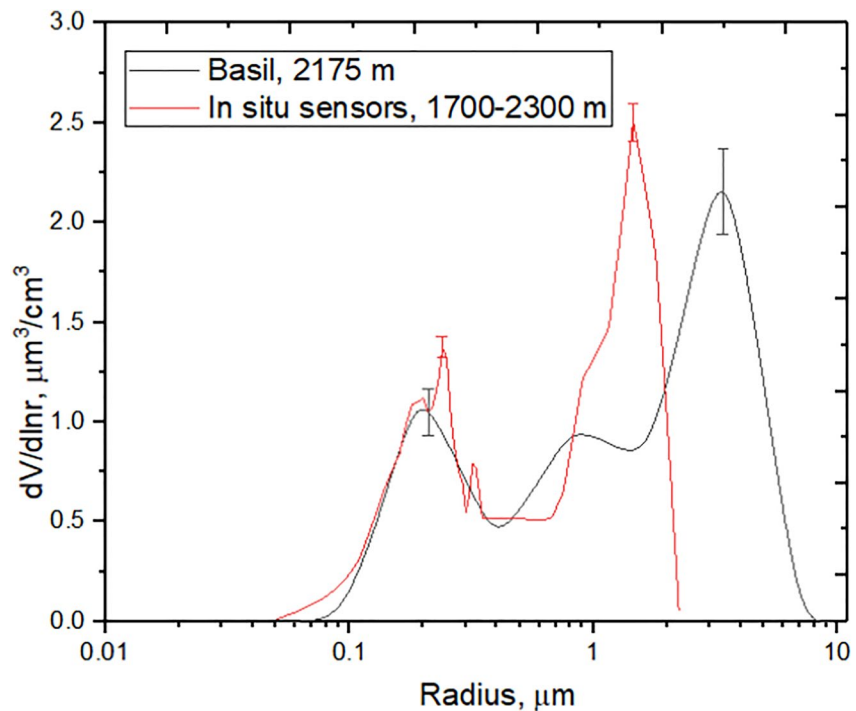
Figure 7. Comparison between BASIL and the aircraft in-situ sensors (SMPS + GRIMM OPC), expressed in terms of effective radius.

are in the range 0.35–0.95 µm. BASIL and the in-situ sensors are found to be in good agreement at all heights, with values measured by the aircraft sensors always within the error bars of the corresponding Raman lidar measurements. The only exception is represented by the data points at ∼4 km. Effective radius values in the elevated aerosol layer are slightly larger than in the lower layer. The discrepancy observed at 4 km is possibly attributable to the lack in measurement sensitivity of in-situ sensors in characterizing aerosol size distributions and microphysical properties in the course mode. In fact, as anticipated above, in-situ sensors have a limited response in the coarse mode domain.

Comparisons between BASIL and the aircraft in-situ sensors were carried out also in terms of particle size distributions. Figure 8 illustrates the aerosol size distribution, expressed in terms of volume concentration, from BASIL at 2,200 m and from the in-situ sensors between 1,700 and 2,300 m. It is to be specified that the aircraft is characterized by an ascent speed of 150 m per minute, with a 4 min temporal integration for size distribution measurements. Such a long integration time is required for the in-situ sensors to provide accurate enough volume concentration size distributed measurements.

Both BASIL and the in-situ sensors reveal the presence of multiple modes. Specifically, BASIL identifies three distinct modes: a fine mode at 0.2 and two coarse modes at 0.8–1.0 and 3–3.5 µm. Small particles (<0.5 µm) are presumably representative of the aerosol fraction from combustion processes (biomass burning in the case of aerosols from North America or coal, oil and oil-shale burning from power plants and industrial areas in North-Eastern Europe). The smaller of the two coarse modes, centered at 0.8–1.0 µm, is possibly associated with a carbon fraction component. Larger particles (>2 µm) are possibly associated with the inorganic aerosol component, with the carbonaceous component typically characterized by smaller sizes than the inorganic fraction (Keene et al., 2007; O'Dowd et al., 2004). Coarse aerosols are generally removed from the atmosphere fairly rapidly by sedimentation. However, advection and convective processes can transport these aerosols for long distances (Heald et al., 2005).

Results in Figure 8 reveal a good agreement between BASIL and the aircraft sensors at 2,200 m. However, at this height a complete separation between the two coarse modes is not captured by the in-situ sensors, whose measurements show the presence of a sort of "merged" mode, with an inflection point around 1 µm. In this regard it is to be again recalled that the in-situ sensors have a very limited sensitivity to particle radii larger than 2 µm and this may obviously lead to a limited response to such particle component when present. This lack of response determines (Figure 8) that the larger of the two coarse modes at 3–3.5 µm retrieved by BASIL generates a fictitious
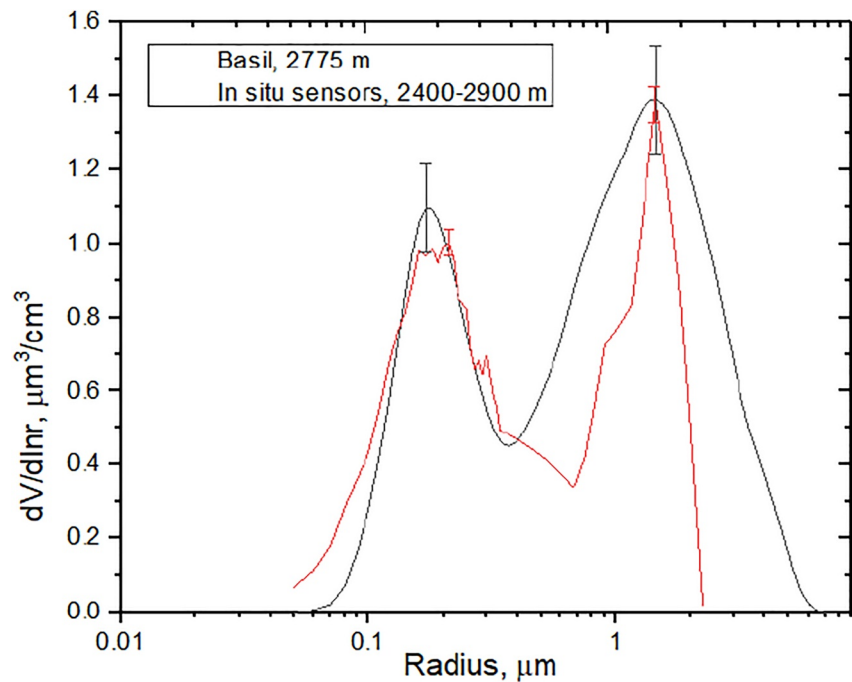
Figure 8. Comparison between BASIL at 2,200 m and the aircraft in-situ sensors (SMPS + GRIMM OPC) in the height interval 1,700–2,300 m, expressed in terms of aerosol volume concentration distribution.

mode in the in-situ measurements around 1.5 μm, with volume concentration values (2.5 μm^3/cm^3) comparable to those measured at the same height by BASIL (2.2 μm^3/cm^3). Conversely, the smaller of the two coarse modes generates an inflection point around 1 μm characterized by a volume concentration value of 1.2 μm^3/cm^3, as opposed to a value of 0.95 μm^3/cm^3 retrieved by BASIL. However, with regard to the fine mode, a very good agreement is present in Figure 8 between BASIL and the in-situ sensors both in terms of radius values (0.2 μm for both sensors) and volume concentration values (1.15 μm^3/cm^3 and 1.20–1.35 μm^3/cm^3).
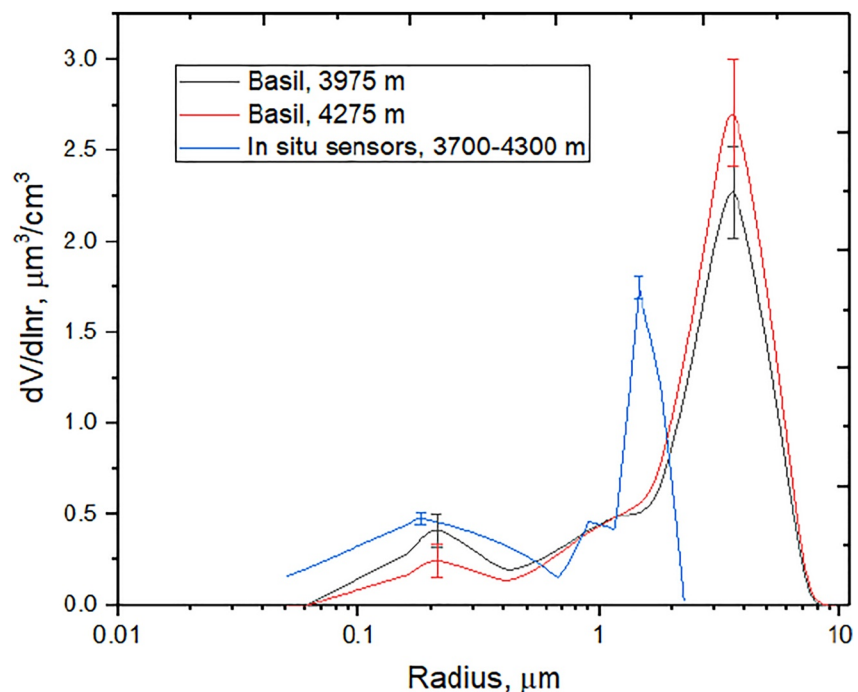
Figure 9 shows the aerosol volume concentration distribution as measured by BASIL at 2,800 m and by the in-situ sensors in the height interval between 2,400 and 2,900 m. The agreement between the two measurements is very good also at this height level, with both the Raman lidar and the in-situ sensors identifying the presence of two modes: a fine mode at 0.2 and a coarse mode at 1.4 μm. For what concerns the fine mode, that is, the aerosol fraction from combustion processes, volume concentration values are similar to those found at 2,200 m, with the Raman lidar and in-situ sensors being in very good agreement (1.1 and 1.0 μm^3/cm^3, respectively). For what concerns the coarse fraction, only the smaller of the two modes observed at 2,200 m is left, probably as a result of sedimentation, this mode being characterized by slightly larger radii (1.4 μm) and larger volume concentration values (1.4 μm^3/cm^3).

Figure 10 shows the aerosol volume concentration distribution as measured by BASIL at 4,000 and 4,300 m and by the in-situ sensors in the height interval between 3,700 and 4,300 m. At these heights, the fine aerosol fraction is considerably reduced. Conversely, the coarse fraction becomes predominant. As extensively illustrated above, the ensemble back-trajectories indicate that air masses observed at these heights were originated approximately 11–12 days earlier over North America. These air masses, after traveling over the Ocean for 8–9 days, overpassed Spain at considerable high heights (∼4,000 m) and therefore were not altered by mixing with any continental or polluted aerosol component. The predominance of the coarse fraction observed in Figure 10 is to be attributed to the prevalence of coarse particles in wildfire smoke (Groβ et al., 2013; Vicente et al., 2013). Additionally, aged smoke particles, with a lifetime exceeding 1 week, having undergone a long-range transport from North America to Europe, are often characterized by size distributions shifted toward increasing particle sizes with increasing residence time in the atmosphere (Ansmann et al., 2021). These represent possible motivations for the predominance of the coarse fraction in the upper layer. Again, a very good agreement is found between the Raman lidar

Figure 9. Comparison between BASIL at 2,800 m and the aircraft in-situ sensors (SMPS + GRIMM OPC) in the height interval 2,400–2,900 m, expressed in terms of aerosol volume concentration distribution.

and the aircraft sensors, with both instruments properly revealing the presence of the fine and the coarse modes. The fine mode is identified at 0.22 μm by BASIL and at 0.18 μm by the in-situ sensors, with volume concentration values from BASIL being 0.25 and 0.4 μm³/cm³ at 4,000 and 4,300 m, respectively. Volume concentration values from the in-situ sensors are not exceeding 0.5 μm³/cm³. These volume concentration values are

Figure 10. Comparison between BASIL at 4,000 and 4,300 m and the aircraft in-situ sensors (SMPS + GRIMM OPC) in the height interval 3,700–4,300 m, expressed in terms of aerosol volume concentration distribution.
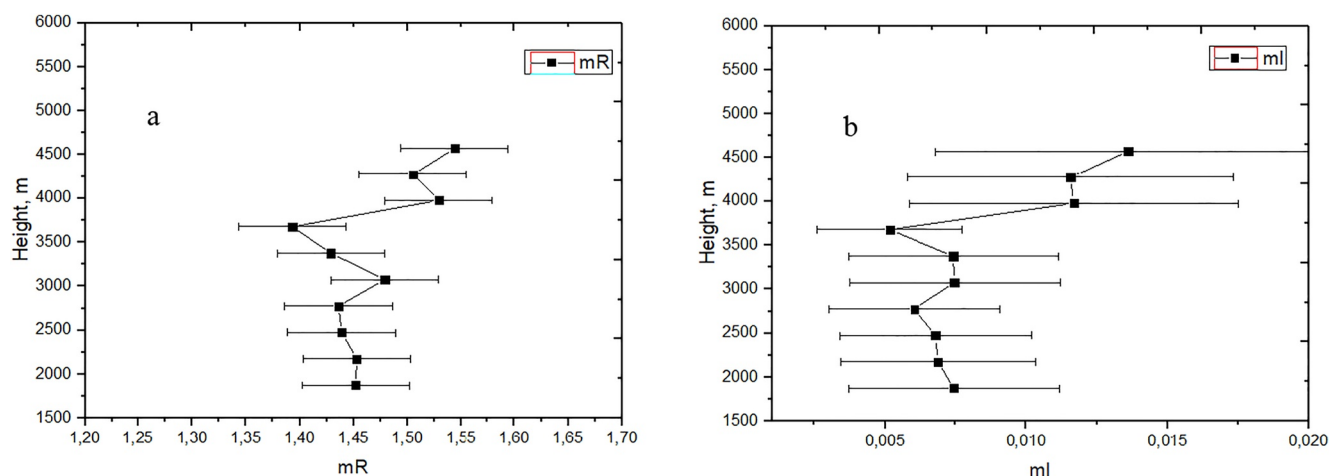
Figure 11. Real (panel a) and imaginary part (panel b) of the particle refractive index.

approximately 2–4 times smaller than those observed at lower heights, due to the progressive reduction of the fine mode fraction with increasing heights.

For what concerns the coarse mode, this is properly identified by BASIL, with peak volume concentration values at 4,000 and 4,300 m being 2.25 and 2.7 $\mu m^3/cm^3$, respectively. Once again, in-situ sensors do not properly reveal this mode contribution as a result of their limited sensitivity to particles with radii exceeding 2 μm.

Two more optical parameters retrieved from the three-wavelength Raman lidar measurements are the real and imaginary part of the particle refractive index. These two quantities are of paramount importance in the assessment of the scattering and absorbing properties of aerosol particles. More specifically, the real part of the refractive index, m_R, quantifies the degree of light bending within the particle, and consequently its contribution to particle scattering, while the imaginary part, m_I, quantifies the light absorption within the particle. Figure 11 shows the height variability of m_R and m_I as retrieved from BASIL measurements. Values of m_R within the lower aerosol layer are in the range 1.39–1.48, with an average value of 1.44, while in the upper layer m_R varies in the range 1.51–1.54, with an average value of 1.53. Additionally, values of m_I within the lower aerosol layer are in the range 0.005–0.0075, with a mean value of 0.0067, while in the upper layer m_I varies in the range 0.011–0.013, with a mean value of 0.0123. In the interpretation of the present results it is to be considered that the retrieval of m_R is characterized by an uncertainty of ± 0.05, while the retrieval of m_I has an uncertainty of $\pm 50\%$. Unfortunately, independent measurements of m_R and m_I from in-situ sensors are not available. However, an indirect estimation of these quantities can be inferred from the compositional information available from the chemical sensor, supported by literature papers (McMeeking, 2004; Mico et al., 2019; Panchenko et al., 2012; Sekiyama et al., 2012; Wang et al., 2021; Willoughby et al., 2017; Zhao et al., 2020).

Indeed, values of m_R retrieved within the lower aerosol layer (1.39–1.48) are found to be compatible with measurements from the chemical sensor. The AMS reveals abundance in this layer of sulfate and organic carbon, whose values of m_R are reported to be 1.43 and 1.53, respectively (Sekiyama et al., 2012). Retrieved values of m_R are also compatible with the back-trajectory analyses as in fact the aerosol presumably originated in North America from biomass burning or in North-Eastern Europe from coal, oil and oil-shale burning in power plants and industrial areas. Furthermore, values of m_R observed in the lower layer are also compatible with those reported for the submicron and coarse fractions of black carbon particles from combustion of coal, oil and oil-shale (1.42–1.45 and 1.50, respectively, Panchenko et al., 2012). Finally, values of m_R within the lower layer are also compatible with smoke particles, with values reported in literature around 1.58 (McMeeking, 2004).

Furthermore, values of m_I retrieved within the lower aerosol layer are compatible with those found for the submicron and coarse fractions of black carbon particles (0.0075 in Panchenko et al., 2012), which can result from combustion of coal, oil and oil-shale. Observed values of m_I are also compatible with mineral dust particles (0.006 in Mico et al., 2019, and Wang et al., 2021, and 0.0055 in Willoughby et al., 2017) and with smoke particles (0.008 in McMeeking, 2004).

As previously anticipated, sounded aerosol particles in the upper aerosol layer are supposedly smoke particles from wildfires. In this respect, McMeeking (2004) reported values of m_R and m_I of 1.577 and 0.008, respectively, for wildfire smoke-influenced aerosols, which are very close to those observed by the Raman lidar in the upper aerosol layer. Similar values (m_R in the range 1.56–1.66 and m_I in the range 0.05–0.07) were reported by Wandinger et al. (2002) for biomass burning and industrial-pollution aerosols in the free troposphere. Additionally, the presence of organic components in the aerosol composition has been identified by the chemical sensor, with values of m_R reported in literature for organic aerosol (1.53 in Sekiyama et al., 2012, and 1.55 in Zhao et al., 2020) being also very close to those found in this aerosol layer. Values of m_I retrieved within the upper aerosol layer (0.011–0.013) are compatible with carbonaceous aerosols including an organic component, with values of m_I found in literature for organic and organic carbon aerosols being around 0.02 (Wang et al., 2021).

Depolarization and lidar ratio profiles from the Raman lidar are included in Figure 3, but no specific use of these quantities has been carried out so far for the purpose of interpreting the results or verifying the considered hypotheses.

The profile of $\delta_{355}(z)$ in Figure 3b) is characterized by small values (smaller than 0.05 or 5%) throughout the sounded vertical region. More specifically, values are in between 2.0% and 2.3% in the lower aerosol layer and in between 2.2% and 3.2% in the upper aerosol layer. Observed values of $\delta_{355}(z)$ are compatible with spherical particles from combustion processes, which underwent aging and a long-range transport from their sources to the observational site. These depolarization values are similar to those reported for smoke particles from wild or forest fires by other authors. Specifically, Müller et al. (2005) reported values in the range 1.5%–3% for free tropospheric aerosol plumes associated with North American forest fire smoke. Low smoke depolarization ratio values (<3%) were also reported by Haarig et al. (2018) at all laser wavelengths from 355 to 1064 nm for aged tropospheric and stratospheric Canadian wildfire smoke.

Observed values of LR_{355} and LR_{532} are in the range 40–50 sr in both the lower and upper aerosol layer, with slightly larger values at 532 than at 355 nm. Values in the lower layer are found to slightly decrease with height from ∼50 to ∼40 sr at both wavelengths, while values in the upper layer do not reveal a specific height trend. Observed lidar ratio values are in agreement with a variety of literature measurements for aged smoke aerosols, with most references reporting slightly larger values at 532 than at 355 nm. Specifically, Ansmann et al. (2021) reported values of LR_{355} around 55 sr and values of LR_{532} around 70 sr for aged smoke particles, Haarig et al. (2018) reported values of LR_{355} in the range 35–50 sr and values of LR_{532} in the range 50–80 sr for aged Canadian smoke particles, Wandinger et al. (2002)) reported values of LR_{355} around 65 sr and values of LR_{532} around 90 sr for aged Canadian smoke particles, while Murayama et al. (2004) reported values of LR_{355} around 40 sr and values of LR_{532} around 65 sr for aged Siberian smoke particles.

5. Summary

The paper illustrates a comparison between Raman lidar retrievals and aircraft in-situ sensors' measurements in terms of a variety of aerosol size and microphysical properties, namely the parameters of a bi-trimodal size distribution, the volume concentration, the effective radius and the real and imaginary part of the refractive index. For the purpose of retrieving aerosol size and microphysical properties, an algorithm based on Tikhonov regularization was applied to the multi-wavelength Raman lidar measurements of the particle backscattering and extinction coefficient profiles. The retrieval scheme also allows us to determine the complex refractive index, which is a parameter unfortunately not measured by the aircraft sensors. The attention was focused on a case study during HyMeX-SOP1 (02 October 2012), with BASIL measurements indicating the presence of a lower aerosol layer extending up to 3.3 km and an elevated layer extending from 3.6 to 4.6 km. Results obtained through the retrieval scheme indicate the presence of a size distribution with two particle modes, in both aerosol layers: a fine mode, with a mean radius of approximately 0.2, and a coarse mode, with mean radii of 2–4 μm. A very good agreement between the lidar and the aircraft sensors is found for all considered parameters. Raman lidar retrievals are used in combination with in-situ sensors' measurements, ensemble back-trajectory analyses from the Lagrangian model HYSPLIT and aerosol composition measurements from the AMS. The combined use of these different data sets allows us to properly assess the different typologies and origin of the two observed aerosol layers.

Retrievals from three-wavelength Raman lidar measurements highlight the high ability of this sensor to properly characterize the size and microphysical properties of aged aerosol particle generated by biomass burning from wildfires in North America and experiencing a long-range oversea transport to the observational site.

Data Availability Statement

The data used in this research effort, together with the related metadata, are available from the public data repository HyMeX database, which is freely accessible by all users through the following link: http://mistrals.sedoo.fr/HyMeX (Di Girolamo, 2022).

References

Albrecht, B. A. (1989). Aerosols, cloud microphysics, and fractional cloudiness. *Science*, *245*(4923), 1227–1230. https://doi.org/10.1126/science.245.4923.1227

Ansmann, A., Ohneiser, K., Mamouri, R.-E., Knopf, D. A., Veselovskii, I., Baars, H., et al. (2021). Tropospheric and stratospheric wildfire smoke profiling with lidar: Mass, surface area, CCN, and INP retrieval. *Atmospheric Chemistry and Physics*, *21*(12), 9779–9807. https://doi.org/10.5194/acp-21-9779-2021

Ansmann, A., Riebesell, M., & Weitkamp, C. (1990). Measurement of atmospheric aerosol extinction profiles with a Raman lidar. *Optics Letters*, *15*(13), 746–748. https://doi.org/10.1364/ol.15.000746

Ansmann, A., Wandinger, U., Riebesell, M., Weitkamp, C., & Michaelis, W. (1992). Independent measurement of extinction and backscatter profiles in cirrus clouds by using a combined Raman elastic-backscatter lidar. *Applied Optics*, *31*(33), 7113–7131. https://doi.org/10.1364/ao.31.007113

Artusa, A. (2012). U.S. Drought monitor, October 2, 2012. *US Ag in Drought Archive*, *31*. Retrieved from http://digitalcommons.unl.edu/droughtarchive/31

Bonsang, B., Polle, C., & Lambert, G. (1992). Evidence for marine production of isoprene. *Geophysical Research Letters*, *19*(11), 1129–1132. https://doi.org/10.1029/92gl00083

Boucher, O., Randall, D., Artaxo, P., Bretherton, C., Feingold, G., Forster, P., et al. (2013). Clouds and aerosols. In T. F. Stocker, D. Qin, G.-K. Plattner, M. Tignor, S. K. Allen, J. Doschung, et al. (Eds.), *Climate change 2013: The physical science basis. Contribution of working group I to the fifth assessment report of the intergovernmental panel on climate change* (pp. 571–657). Cambridge University Press. https://doi.org/10.1017/CBO9781107415324.016

Burton, S. P., Ferrare, R. A., Hostetler, C. A., Hair, J. W., Rogers, R. R., Obland, M. D., et al. (2012). Aerosol classification using airborne High Spectral Resolution Lidar measurements – Methodology and examples. *Atmospheric Measurement Techniques*, *5*(1), 73–98. https://doi.org/10.5194/amt-5-73-2012

Canagaratna, M. R., Jayne, J. T., Jimenez, J. L., Allan, J. D., Alfarra, M. R., Zhang, Q., et al. (2007). Chemical and microphysical characterization of ambient aerosols with the aerodyne aerosol mass spectrometer. *Mass Spectrometry Reviews*, *26*(2), 185–222. https://doi.org/10.1002/mas.20115

Carter, W. P. (1994). Development of ozone reactivity scales for volatile organic compounds. *Air & Waste*, *44*(7), 881–899. https://doi.org/10.1080/1073161X.1994.10467290

Charlson, R. J., Schwartz, S. E., Hales, J. M., Cess, R. D., Coakley, J. A., Hansen, J. E., & Hofmann, D. J. (1992). Climate forcing by anthropogenic aerosols. *Science*, *255*(5043), 423–430. https://doi.org/10.1126/science.255.5043.423

Crumeyrolle, S., Manninen, H. E., Sellegri, K., Roberts, G., Gomes, L., Kulmala, M., et al. (2010). New particle formation events measured on board the ATR-42 aircraft during the EUCAARI campaign. *Atmospheric Chemistry and Physics*, *10*(14), 6721–6735. https://doi.org/10.5194/acp-10-6721-2010

De Rosa, B., Di Girolamo, P., & Summa, D. (2018). Characterization of atmospheric thermodynamic variables by Raman lidar in the frame of the international network for the detection of atmospheric composition change – NDACC. *EPJ Web of Conferences*, *176*(2018), 04010. https://doi.org/10.1051/epjconf/201817604010

De Rosa, B., Di Girolamo, P., & Summa, D. (2020). Temperature and water vapour measurements in the framework of the network for the detection of atmospheric composition change (NDACC). *Atmospheric Measurement Techniques*, *13*(2), 405–427. https://doi.org/10.5194/amt-13-405-2020

De Rosa, B., Di Girolamo, P., Summa, D., Flamant, C., Bousquet, O., Cacciani, M., & Stelitano, D. (2018). Temperature inter-comparison effort in the framework of hydrological cycle in the mediterranean experiment – Special Observation Period (HyMeX-SOP1). *EPJ Web of Conferences*, *176*(2018), 08010. https://doi.org/10.1051/epjconf/201817608010

Di Girolamo, P. (2022). Particle backscattering and extinction coefficient at 355 mm, Particle backscattering and extinction coefficient at 532 mm, Particle backscattering coefficient at 1064 mm. [Data set]. HyMeX Database. Retrieved from http://mistrals.sedoo.fr/HyMeX/

Di Girolamo, P., Ambrico, P. F., Amodeo, A., Boselli, A., Pappalardo, G., & Spinelli, N. (1999). Aerosol observations by lidar in the nocturnal boundary layer. *Applied Optics*, *38*(21), 4585–4595. https://doi.org/10.1364/AO.38.004585

Di Girolamo, P., Behrendt, A., Kiemle, C., Wulfmeyer, V., Bauer, H., Summa, D., et al. (2008). Simulation of satellite water vapourlidar measurements: Performance assessment under real atmospheric conditions. *Remote Sensing of Environment*, *112*(4), 1552–1568. https://doi.org/10.1016/j.rse.2007.08.008

Di Girolamo, P., Behrendt, A., & Wulfmeyer, V. (2006). Spaceborne profiling of atmospheric temperature and particle extinction with pure rotational Raman lidar and of relative humidity in combination with differential absorption lidar: Performance simulations. *Applied Optics*, *45*(11), 2474–2494. https://doi.org/10.1364/AO.45.002474

Di Girolamo, P., De Rosa, B., Flamant, C., Summa, D., Bousquet, O., Chazette, P., et al. (2020). Water vapor mixing ratio and temperature inter-comparison results in the framework of the hydrological cycle in the mediterranean experiment—Special Observation Period 1. *Bulletin of Atmospheric Science and Technology*, *1*(2), 113–153. https://doi.org/10.1007/s42865-020-00008-3

Di Girolamo, P., Gagliardi, R. V., Pappalardo, G., Spinelli, N., Velotta, R., & Berardi, V. (1995). Two wavelength Lidar analysis of stratospheric aerosol size distribution. *Journal of Aerosol Science*, *26*(6), 989–1001. https://doi.org/10.1016/0021-8502(95)00025-8

Di Girolamo, P., Marchese, R., Whiteman, D. N., & Demoz, B. B. (2004). Rotational Raman Lidar measurements of atmospheric temperature in the UV. *Geophysical Research Letters*, *31*(1), L01106. https://doi.org/10.1029/2003GL018342

Di Girolamo, P., Scoccione, A., Cacciani, M., Summa, D., De Rosa, B., & Schween, J. H. (2018). Clear-air lidar dark band. *Atmospheric Chemistry and Physics*, *18*(7), 4885–4896. https://doi.org/10.5194/acp-18-4885-2018

Di Girolamo, P., Summa, D., Bhawar, R., Di Iorio, T., Cacciani, M., Veselovskii, I., et al. (2012). Raman lidar observations of a Saharan dust outbreak event: Characterization of the dust optical properties and determination of particle size and microphysical parameters. *Atmospheric Environment*, *50*, 66–78. https://doi.org/10.1016/j.atmosenv.2011.12.061

Di Girolamo, P., Summa, D., Cacciani, M., Norton, E. G., Peters, G., & Dufournet, Y. (2012). Lidar and radar measurements of the melting layer: Observations of dark and bright band phenomena. *Atmospheric Chemistry and Physics*, *12*(9), 4143–4157. https://doi.org/10.5194/acp-12-4143-2012

Di Girolamo, P., Summa, D., & Ferretti, R. (2009). Multiparameter Raman lidar measurements for the characterization of a dry stratospheric intrusion event. *Journal of Atmospheric and Oceanic Technology*, *26*(9), 1742–1762. https://doi.org/10.1175/2009JTECHA1253.1

Draxler, R. R., & Hess, G. D. (1998). An overview of the HYSPLIT_4 modeling system for trajectories, dispersion and deposition. *Australian Meteorological Magazine*, *47*, 295–308.

Drewnick, F., Hings, S. S., DeCarlo, P., Jayne, J. T., Gonin, M., Fuhrer, K., et al. (2005). A new time-of-flight aerosol mass spectrometer (TOF-AMS)—Instrument description and first field deployment. *Aerosol Science and Technology*, *39*(7), 637–658. https://doi.org/10.1080/02786820500182040

Elterman, L. (1966). Aerosol measurements in the troposphere and stratosphere. *Applied Optics*, *5*(11), 1769–1776. https://doi.org/10.1364/ao.5.001769

Fernald, F. G. (1984). Analysis of atmospheric lidar observations: Some comments. *Applied Optics*, *23*(5), 652–653. https://doi.org/10.1364/ao.23.000652

Fiocco, G., & Grams, G. (1964). Observations of the aerosol layer at 20 km by optical radar. *Journal of the Atmospheric Sciences*, *21*(3), 323–324. https://doi.org/10.1175/1520-0469(1964)021<0323:ootala>2.0.co;2

Freudenthaler, V., Esselborn, M., Wiegner, M., Heese, B., Tesche, M., Ansmann, A., et al. (2009). Depolarization ratio profiling at several wavelengths in pure Saharan dust during SAMUM 2006. *Tellus B: Chemical and Physical Meteorology*, *61*(1), 165–179. https://doi.org/10.1111/j.1600-0889.2008.00396.x

Groß, S., Esselborn, M., Weinzierl, B., Wirth, M., Fix, A., & Petzold, A. (2013). Aerosol classification by airborne high spectral resolution lidar observations. *Atmospheric Chemistry and Physics*, *13*(5), 2487–2505. https://doi.org/10.5194/acp-13-2487-2013

Guerra, S. A., Olsen, S. R., & Anderson, J. J. (2014). Evaluation of the SO2 and NOx offset ratio method to account for secondary PM2.5 formation. *Journal of the Air & Waste Management Association*, *64*(3), 265–271. https://doi.org/10.1080/10962247.2013.852636

Haarig, M., Ansmann, A., Baars, H., Jimenez, C., Veselovskii, I., Engelmann, R., & Althausen, D. (2018). Depolarization and lidar ratios at 355, 532, and 1064 nm and microphysical properties of aged tropospheric and stratospheric Canadian wildfire smoke. *Atmospheric Chemistry and Physics*, *18*(16), 11847–11861. https://doi.org/10.5194/acp-18-11847-2018

Heald, C. L., Jacob, D. J., Park, R. J., Russell, L. M., Huebert, B. J., Seinfeld, J. H., et al. (2005). A large organic aerosol source in the free troposphere missing from current models. *Geophysical Research Letters*, *32*(18), L18809. https://doi.org/10.1029/2005gl023831

Heim, M., Mullins, B. J., Umhauera, H., & Kaspera, G. (2008). Performance evaluation of three optical particle counters with an efficient "multimodal" calibration method. *Journal of Aerosol Science*, *39*(12), 1019–1031. https://doi.org/10.1016/j.jaerosci.2008.07.006

Illingworth, A. J., Barker, H. W., Beljaars, A., Ceccaldi, M., Chepfer, H., Clerbaux, N., et al. (2015). The EarthCARE satellite: The next step forward in global measurements of clouds, aerosols, precipitation, and radiation. *Bulletin America Meteorology Social*, *96*(8), 1311–1332. https://doi.org/10.1175/bams-d-12-00227.1

IPCC. (2007). Summary for policy makers. In S. Solomon, D. Qin, & M. Manning (Eds.), *Climate change 2007: The physical science basis*, *Contribution of working group I to the fourth assessment report of the intergovernmental panel on climate change*. Cambridge University Press.

Keene, W. C., Maring, H., Maben, J. R., Kieber, D. J., Pszenny, A. A. P., Dahl, E. E., et al. (2007). Chemical and physical characteristics of nascent aerosols produced by bursting bubbles at a model air-sea interface. *Journal of Geophysical Research*, *112*, D21202. https://doi.org/10.1029/2007jd008464

Khain, A., Pokrovsky, A., & Sednev, I. (1999). Some effects of cloud–aerosol interaction on cloud microphysics structure and precipitation formation: Numerical experiments with a spectral microphysics cloud ensemble model. *Atmospheric Research*, *52*(3), 195–220. https://doi.org/10.1016/s0169-8095(99)00027-7

Kim, H., Zhang, Q., & Heo, J. (2018). Influence of intense secondary aerosol formation and long-range transport on aerosol chemistry and properties in the seoul metropolitan area during spring time: Results from KORUSAQ. *Atmospheric Chemistry and Physics*, *18*(10), 7149–7168. https://doi.org/10.5194/acp-18-7149-2018

Klett, J. D. (1981). Stable analytical inversion solution for processing lidar returns. *Applied Optics*, *20*(2), 211–220. https://doi.org/10.1364/ao.20.000211

Klett, J. D. (1985). Lidar inversion with variable backscatter/extinction ratios. *Applied Optics*, *24*(11), 1638–1643. https://doi.org/10.1364/ao.24.001638

Leck, C., & Bigg, E. K. (2005a). Biogenic particles in the surface microlayer and overlaying atmosphere in the central Arctic Ocean during summer. *Tellus, Series B*, *57*(4), 305–316. https://doi.org/10.1111/j.1600-0889.2005.00148.x

Leck, C., & Bigg, E. K. (2005b). Source and evolution of the marine aerosol—A new perspective. *Geophysical Research Letters*, *32*(19), L19803. https://doi.org/10.1029/2005gl023651

Marais, E. A., Jacob, D. J., Jimenez, J. L., Campuzano-Jost, P., Day, D. A., Hu, W., et al. (2016). Aqueous-phase mechanism for secondary organic aerosol formation from isoprene: Application to the southeast United States and co-benefit of SO2 emission controls. *Atmospheric Chemistry and Physics*, *16*(3), 1603–1618. https://doi.org/10.5194/acp-16-1603-2016

McMeeking, G. R. (2004). *Size distribution measurements of wildfire smoke-influences aerosol at Yosemite National Park, Colorado State University*. Department of Atmospheric Science, Colorado State University.

Mico, S., Deda, A., Tsaousi, E., Alushllari, M., & Pomonis, P. (2019). Complex refractive index of aerosol samples, women in physics. *AIP Conference Proceedings*, *2109*, 1–4. https://doi.org/10.1063/1.5110120

Müller, D., Ansmann, A., Mattis, I., Tesche, M., Wandinger, U., Althausen, D., & Pisani, G. (2007). Aerosol-type-dependent lidar ratios observed with Raman lidar. *Journal of Geophysical Research*, *112*, D16202. https://doi.org/10.1029/2006jd008292

Müller, D., Mattis, I., Wandinger, U., Ansmann, A., Althausen, D., & Stohl, A. (2005). Raman lidar observations of aged Siberian and Canadian forest fire smoke in the free troposphere over Germany in 2003: Microphysical particle characterization. *Journal of Geophysical Research*, *110*, D17201. https://doi.org/10.1029/2004JD005756

Müller, D., Wandinger, U., & Ansmann, A. (1999). Microphysical particle parameters from extinction and backscatter lidar data by inversion with regularization: Simulation. *Applied Optics*, *38*(12), 2358–2368. https://doi.org/10.1364/ao.38.002358

Murayama, T., Müller, D., Wada, K., Shimizu, A., Sekiguchi, M., & Tsukamoto, T. (2004). Characterization of Asian dust and Siberian smoke with multi-wavelength Raman lidar over Tokyo, Japan in spring 2003. *Geophysical Research Letters*, *31*(23), L23103. https://doi.org/10.1029/2004GL021105

NOAA, W. (2012). February US release: Tue, 8 Mar 2013.11.

O'Dowd, C. D., Facchini, M. C., Cavalli, F., Ceburnis, D., Mircea, M., Decesari, S., et al. (2004). Biogenically driven organic contribution to marine aerosol. *Nature*, *431*(7009), 676–680. https://doi.org/10.1038/nature02959

Panchenko, M. V., Zhuravleva, T. B., Terpugova, S. A., Polkin, V. V., & Kozlov, V. S. (2012). An empirical model of optical and radiative characteristics of the tropospheric aerosol over West Siberia in summer. *Atmospheric Measurement Techniques*, *5*(7), 1513–1527. https://doi.org/10.5194/amt-5-1513-2012

Rap, A., Scott, C. E., Spracklen, D. V., Bellouin, N., Forster, P. M., Carslaw, K. S., et al. (2013). Natural aerosol direct and indirect radiative effects. *Geophysical Research Letters*, *40*(12), 3297–3301. https://doi.org/10.1002/grl.50441

Rolph, G., Stein, A., & Stunder, B. (2017). Real-time environmental applications and display system: READY. *Environmental Modelling & Software*, *95*, 210–228. https://doi.org/10.1016/j.envsoft.2017.06.025

Sekiyama, T. T., Tanaka, T. Y., & Miyoshi, T. (2012). A simulation study of the ensemble-based data assimilation of satellite-borne lidar aerosol observations. *Geoscientific Model Development Discussions*, *5*, 1877–1947. https://doi.org/10.5194/gmdd-5-1877-2012

Stein, A. F., Draxler, R. R., Rolph, G. D., Stunder, B. J. B., Cohen, M. D., & Ngan, F. (2015). NOAA's HYSPLIT atmospheric transport and dispersion modeling system. *Bulletin of the American Meteorological Society*, *96*(12), 2059–2077. https://doi.org/10.1175/BAMS-D-14-00110.1

Stohl, A. (1998). Computation, accuracy and applications of trajectories—A review and bibliography. *Atmospheric Environment*, *32*(6), 947–966. https://doi.org/10.1016/S1352-2310(97)00457-3

Stohl, A., Eckhardt, S., Forster, C., James, P., Spichtinger, N., & Seibert, P. (2002). A replacement for simple back trajectory calculations in the interpretation of atmospheric trace substance measurements. *Atmospheric Environment*, *36*(29), 4635–4648. https://doi.org/10.1016/s1352-2310(02)00416-8

Sullivan, A. P., May, A. A., Lee, T., McMeeking, G. R., Kreidenweis, S. M., Akagi, S. K., et al. (2014). Airborne characterization of smoke marker ratios from prescribed burning. *Atmospheric Chemistry and Physics*, *14*(19), 10535–10545. https://doi.org/10.5194/acp-14-10535-2014

Summa, D., Di Girolamo, P., Flamant, C., De Rosa, B., Cacciani, M., & Stelitano, D. (2018). Water vapour inter-comparison effort in the framework of the hydrological cycle in the mediterranean experiment – Special observation period (hymex-sop1). *EPJ Web of Conferences*, *176*(2018), 08016. https://doi.org/10.1051/epjconf/201817608016

Thompson, G., & Eidhammer, T. (2014). A study of aerosol impacts on clouds and precipitation development in a large winter cyclone. *Journal of the Atmospheric Sciences*, *71*(10), 3636–3658. https://doi.org/10.1175/jas-d-13-0305.1

Twomey, S. (1977). The influence of pollution on the shortwave albedo of clouds. *Journal of the Atmospheric Sciences*, *34*(7), 1149–1152. https://doi.org/10.1175/1520-0469(1977)034<1149:tiopot>2.0.co;2

Veselovskii, I., Dubovik, O., Kolgotin, A., Korenskiy, M., Whiteman, D. N., Allakhverdiev, K., & Huseyinoglu, F. (2012). Linear estimation of particle bulk parameters from multi-wavelength lidar measurements. *Atmospheric Measurement Techniques*, *5*, 1135–1145. https://doi.org/10.5194/amt-5-1135-2012

Veselovskii, I., Dubovik, O., Kolgotin, A., Lapyonok, T., Di Girolamo, P., Summa, D., et al. (2010). Application of randomly oriented spheroids for retrieval of dust particle parameters from multi-wavelength lidar measurements. *Journal of Geophysical Research*, *115*, D21203. https://doi.org/10.1029/2010JD014139

Veselovskii, I., Goloub, P., Podvin, T., Tanre, D., da Silva, A., Colarco, P., et al. (2018). Characterization of smoke and dust episode over west Africa: Comparison of MERRA-2 modeling with multiwavelength mie-Raman lidar observations. *Atmospheric Measurement Techniques*, *11*(2), 949–969. https://doi.org/10.5194/amt-11-949-2018

Veselovskii, I., Kolgotin, A., Griaznov, V., Müller, D., Wandinger, U., & Whiteman, D. (2002). Inversion with regularization for the retrieval oftropospheric aerosol parameters from multi-wavelength lidar sounding. *Applied Optics*, *41*(18), 3685–3699. https://doi.org/10.1364/ao.41.003685

Vicente, A., Alves, C., Calvo, A. I., Fernandes, A. P., Nunes, T., Monteiro, C., et al. (2013). Emission factors and detailed chemical composition of smoke particles from the 2010 wildfire season. *Atmospheric Environment*, *71*, 295–303. https://doi.org/10.1016/j.atmosenv.2013.01.062

Wandinger, U., Muller, D., Bockmann, C., Althausen, D., Matthias, V., Bosenberg, J., et al. (2002). Optical and microphysical characterization of biomass-burning and industrial-pollution aerosols from multiwavelength lidar and aircraft measurements. *Journal of Geophysical Research*, *107*, 1–20. https://doi.org/10.1029/2000JD000202

Wang, S., Crumeyrolle, S., Zhao, W., Xu, X., Fang, B., Derimian, Y., et al. (2021). Real-time retrieval of aerosol chemical composition using effective density and the imaginary part of complex refractive index. *Atmospheric Environment*, *245*, 117959. https://doi.org/10.1016/j.atmosenv.2020.117959

Willoughby, R. E., Cotterell, M. I., Lin, H., Orr-Ewing, A. J., & Reid, J. P. (2017). Measurements of the imaginary component of the refractive index of weakly absorbing single aerosol particles. *Journal of Physical Chemistry A*, *121*(30), 5700–5710. https://doi.org/10.1021/acs.jpca.7b05418

Wulfmeyer, V., Bauer, H., Di Girolamo, P., & Serio, C. (2005). Comparison of active and passive water vapor remote sensing from space: An analysis based on the simulated performance of IASI and space borne differential absorption lidar. *Remote Sensing of Environment*, *95*(2), 211–230. https://doi.org/10.1016/j.rse.2004.12.019

Yang, W., Li, J., Wang, M., Sun, Y., & Wang, Z. (2018). A case study of investigating secondary organic aerosol formation pathways in Beijing using an observation-based SOA box model. *Aerosol and Air Quality Research*, *18*(7), 1606–1616. https://doi.org/10.4209/aaqr.2017.10.0415

Zhao, D., Yin, Y., Zhang, M., Wang, H., Lu, C., Yuan, L., & Shi, S. (2020). The optical properties of aerosols at the summit of mount Tai in May and June and the retrieval of the complex refractive index. *Atmosphere*, *11*(6), 655. https://doi.org/10.3390/atmos11060655